ELSEVIER

Chemical Engineering Journal 116 (2006) 25–37

Chemical Engineering Journal

www.elsevier.com/locate/cej

Catalytic oxidation of NO by activated carbon fiber (ACF)

Sudhakar Adapa [a], Vivekanand Gaur [b], Nishith Verma [b,*]

[a] *Department of Environmental Engineering, Indian Institute of Technology Kanpur, Kanpur 208016, India*
[b] *Department of Chemical Engineering, Indian Institute of Technology Kanpur, Kanpur 208016, India*

Received 29 May 2005; received in revised form 14 October 2005; accepted 19 October 2005

Abstract

Catalytic oxidation of NO was carried out on activated carbon fibers (ACFs) based on various precursors in a packed bed tubular reactor under varying reaction temperatures (30–80 °C) and inlet NO (100–400 ppm) and O_2 (5–100%) concentrations. Maximum conversion of NO was obtained at the reaction temperature of 30 °C and with increasing O_2 concentrations. The performance of the phenolic resin-based ACF was found to be superior to that of the viscose rayon and pitch-based ACFs. The phenolic resin-based ACF samples were also synthesized in the laboratory by carrying out carbonization and activation of the corresponding raw carbonaceous fibers under varying activation temperatures (800–1000 °C), activation agents (CO_2 and steam) and activation time (30–90 min). The results of the surface characterization of ACF in relation to their oxidation characteristics revealed that the oxidation of NO was favored on the ACF samples having relatively lesser extent of the CO evolving surface O_2 functional groups. A surface kinetic mechanism for the oxidation of NO was proposed and incorporated in a transport model developed to explain the experimental breakthrough data.

Keywords: Activated carbon fibers; Activation; Oxidation; Modeling; Kinetics

1. Introduction

Despite the extensive research efforts on the development of new processes and materials in the field of environmental pollution control, nitrogen oxides (NO_x) emission is still a global issue of increasing concern. Selective catalytic reduction (SCR) is widely used process for the de-nitrification of the flue gas, although this process has several drawbacks, such as high reaction temperature (>300 °C) and un-reacted reducing agents [1]. A number of common adsorbents, including activated carbons may be employed for the removal of NO_2. However, the extent of physical adsorption of NO on activated carbons is generally low because NO is a supercritical fluid at the ambient temperature and the physical adsorption of supercritical fluids is limited due to the weak interactions between the adsorbent and adsorbate [2]. It is in this context that the catalytic oxidation of NO to NO_2 at ambient temperature appears to be promising for the control of NO emissions, since NO_2 can be subsequently removed by adsorption using common adsorbents or by absorbing it in water [3–5]. Here, it may be pointed out that there are few studies reported in open literature, which are concerned with the adsorption of NO, however, mostly on granular activated carbons [6–8].

The present study primarily focuses on the catalytic oxidation of NO to NO_2 by activated carbon fiber (ACF) at room temperature. Although activated carbons in granular form have been the focus of numerous studies in the past, new forms of activated carbon, for example, fiber, cloth, and felt were introduced only in the last decade. ACF has been the focus of recent research due to its micro porous texture having large BET area, significant adsorption characteristics for a number of air pollutant species, and ability of regeneration with ease. In addition, ACFs have flexibility to be applied in reactors, where they can be wrapped or rolled easily. In the present work, the oxidation of NO by O_2 was carried out in a tubular reactor packed with ACF. The reaction temperatures, the gas inlet compositions (NO and O_2), and gas flow rates were varied to ascertain the effects of these operating variables on the extent of oxidation. The effects of the types of precursors (viscose rayon and phenolic resin) on the catalytic activities of ACF were also ascertained. A mechanism for the surface reactions involving NO and O_2 was proposed. The overall kinetic rate expression obtained for the oxidation of NO into NO_2 was incorporated in a mathematical model developed to explain the transient experimental data (breakthrough

* Corresponding author. Tel.: +91 512 2597704; fax: +91 512 2590104.
E-mail address: nishith@iitk.ac.in (N. Verma).

1385-8947/$ – see front matter © 2005 Elsevier B.V. All rights reserved.
doi:10.1016/j.cej.2005.10.007

Nomenclature

a'	total adsorption surface area per unit volume of the fiber (m^{-1})
a_f	external surface area per unit volume of the fiber (m^{-1})
C	concentration (mol/m^3)
C_G	gas phase concentration in the bed (mol/m^3)
C_p	concentration of species at a location r inside the pores (mol/m^3)
C_s	surface concentration of adsorbed species inside the pores (mol/m^2)
d_{bed}	bed diameter (m)
d_f	fiber diameter (m)
D_{comb}	combined pore diffusivity (m^2/s)
D_{eff}	effective pore diffusivity inside pore (m^2/s)
D_k	Knudsen diffusivity (m^2/s)
D_m	molecular diffusivity (m^2/s)
D_z	axial dispersion coefficient (m^2/s)
k_m	particle mass transfer coefficient (m/s)
L	bed length (m)
M	molecular weight of gas (kg/kg mol)
N_r	molar diffusional flux of the component in the radial direction (mol/m^2 s)
Q	volumetric flow rate of the gas (slpm)
r_{pore}	pore radius (m)
R_b	radius of bed (m)
R_f	fiber radius (m)
Re	Reynolds number, $\rho v d_f/\mu$
S	slope of linear isotherm (m^3/kg)
Sc	Schmidt number, $\mu/\rho D_m$
Sh	Sherwood number, $k_m d_f/D_m$
t	time (s)
T	temperature (°C)
V_z	gas velocity in the axial direction (m/s)
W	amount of adsorbent (g)

Greek letters

α	intrafiber porosity
ε_b	bed porosity
μ	gas viscosity (Pa s)
ρ_b	bulk density of fiber (kg/m^3)
ρ_g	gas density (kg/m^3)
τ	tortuosity factor

Subscripts

f	fiber
p	pore of the fiber
r	radial direction of the pore of the fiber

Superscripts

s	at the fiber outer surface
–	volume average quantities inside the pores of particle

curve) obtained during the oxidation of NO by ACF in the packed tubular reactor. From the perspective of practical application, a practical model should also consider the adsorption of moisture and possibly other atmospheric pollutant species such as VOC, SO_2, etc., since an effluent gas typically consists of many of these species. In this study, our main aim is to analyze the adsorptive and catalytic properties of ACF for the control of NO only. The effect of moisture on NO adsorptive characteristics requires a separate study, which is currently underway. This study also includes correlating the surface characteristics of ACFs synthesized from the raw carbonaceous non-activated fibers under varying activation conditions, to their oxidation behavior for NO. The raw carbon fibers were carbonized in the laboratory and subsequently activated by the physical activation method using CO_2 or steam as activation agents under varying activation temperatures and times. The laboratory prepared ACF samples were characterized for their BET area, pore size distribution (PSD), and surface O_2 functional groups and these surface characteristics are discussed in relation to the experimental breakthrough curves obtained during the oxidation of NO.

2. Theoretical analysis

2.1. Kinetic study

We have taken into account two possible states of O_2, either dissociately adsorbed on the surface or molecular in the gaseous phase, in the mechanism for the oxidation of NO by ACF. As per the Langmuir–Hinshelwood model (mechanism 1), gaseous NO and O_2 are assumed to adsorb on the vacant active sites of ACF, followed by oxidation of NO into adsorbed NO_2. The adsorbed NO_2 may further react and form various intermediates such as, NO_3 and NO–NO_3 in adsorbed phase. Finally, the adsorbed intermediate NO–NO_3 is desorbed into NO_2 from the surface, thereby releasing the vacant sites for the adsorption of successive molecules of adsorbates. In accordance with the Eley–Rideal model (mechanism 2), adsorbed NO is assumed to react with the gaseous O_2 (instead of adsorbed O_2) and yield adsorbed NO_2. The subsequent reactions of adsorbed NO_2 are proposed to proceed similar to those outlined for mechanism 1. The overall sequential reactions may be written as follows:

Mechanism 1	Mechanism 2
$NO + C_f \underset{k_{-1}}{\overset{k_1}{\rightleftarrows}} C\text{–}NO$ (a)	$NO + C_f \underset{k_{-1}}{\overset{k_1}{\rightleftarrows}} C\text{–}NO$ (a)
$O_2 + 2C_f \underset{k_{-2}}{\overset{k_2}{\rightleftarrows}} 2C\text{–}O$ (b)	$2C\text{–}NO + O_2 \underset{k_{-2}}{\overset{k_2}{\rightleftarrows}} 2C\text{–}NO_2$ (b)
$C\text{–}NO + C\text{–}O \underset{k_{-3}}{\overset{k_3}{\rightleftarrows}} C\text{–}NO_2 + C_f$ (c)	$C\text{–}NO_2 + C\text{–}NO_2 \underset{k_{-3}}{\overset{k_3}{\rightleftarrows}} C\text{–}NO_3 + NO + C_f$ (c)
$C\text{–}NO_2 + C\text{–}NO_2 \underset{k_{-4}}{\overset{k_4}{\rightleftarrows}} C\text{–}NO_3 + NO + C_f$ (d)	$C\text{–}NO_3 + C\text{–}NO \underset{k_{-4}}{\overset{k_4}{\rightleftarrows}} C\text{–}NO\text{–}NO_3 + C_f$ (d)
$C\text{–}NO_3 + C\text{–}NO \underset{k_{-5}}{\overset{k_5}{\rightleftarrows}} C\text{–}NO\text{–}NO_3 + C_f$ (e)	$C\text{–}NO\text{–}NO_3 \xrightarrow{k_5} 2NO_2 + C_f$ (e)

Mechanism 1	Mechanism 2
$C–NO–NO_3 \xrightarrow{k_6} 2NO_2 + C_f$ (f)	

Here, k_i and k_{-i} ($i = 1$–6) are the forward- and backward-reaction rate constants of respective reactions. C_f denotes the vacant sites, whereas C–NO, C–O, C–NO_2, C–NO_3 and C–NO–NO_3 represent the adsorbed species on the surface of ACF. In mechanism 1, assuming that the desorption of NO_2 (reaction (f)) is the rate-limiting step, the apparent rate of overall reaction may be written as follows:

$$\frac{1}{2}\frac{dC_{NO_2}}{dt} = -\frac{1}{2}\frac{dC_{NO}}{dt} = k_6[C–NO–NO_3] \quad (1)$$

As a consequence, assuming reactions (a)–(e) to be in quasi-equilibrium, the steady-state concentrations of different adsorbed species are obtained as:

$$[C–NO] = K_1 C_{NO}(C_f) \quad (2)$$

$$[C–O] = (K_2 C_{O_2})^{1/2}[C_f] \quad (3)$$

$$[C–NO_2] = \frac{K_3[C–NO][C–O]}{[C_f]} \quad (4)$$

$$[C–NO_3] = \frac{K_4[C–NO_2]^2}{C_{NO}[C_f]} \quad (5)$$

$$[C–NO–NO_3] = \frac{K_5[C–NO_3][C–NO]}{[C_f]} \quad (6)$$

where $K_i = k_i/k_{-i}$ represents the ratio of the forward to backward rate constants of the respective reactions. Using site balance, the total number of sites $[C_t]$ is written as follows:

$$[C_t] = [C_f] + [C–O] + [C–NO] + [C–NO_2] + [C–NO_3] + [C–NO–NO_3] \quad (7)$$

Combining Eqs. (1)–(7), the rate of the removal of NO may be written as:

$$-\frac{1}{2}\frac{dC_{NO}}{dt} = \frac{K_{11}C_{NO}^2}{K_{22} + K_{33}C_{NO} + K_{44}C_{NO}^2} \quad (8)$$

where

$$K_{11} = k_6 K_1^3 K_2 K_3^2 K_4 K_5 [C_f] C_{O_2} \quad (9)$$

$$K_{22} = 1 + K_2^{1/2} C_{O_2}^{1/2} \quad (10)$$

$$K_{33} = K_1 + K_1 K_2^{1/2} K_3 C_{O_2}^{1/2} + K_4 K_3^2 K_2 K_1^2 C_{O_2} \quad (11)$$

$$K_{44} = K_1^3 K_2 K_3^2 K_4 K_5 C_{O_2} \quad (12)$$

Since NO concentration in the inlet stream is smaller compared to O_2, we may neglect C_{NO}^2 term and assume C_{O_2} to be constant in Eq. (8). Therefore, Eq. (8) is further simplified as follows:

$$-\frac{1}{2}\frac{dC_{NO}}{dt} = \frac{rc_1 C_{NO}^2}{1 + rc_2 C_{NO}} \quad (13)$$

where

$$rc_1 = \frac{K_{11}}{K_{22}} \quad \text{and} \quad rc_2 = \frac{K_{33}}{K_{22}} \quad (14)$$

For mechanism 2, assuming reaction (e) to be the rate-controlling step, the rate expression for the oxidation of NO was determined by the same procedure as outlined for the case of mechanism 1. The final expression was mathematically obtained similar to Eq. (13), with difference in the values of rc_1 and rc_2 obtained as follows:

$$rc_1 = K_{11} \quad \text{and} \quad rc_2 = K_{22}$$

where

$$K_{11} = k_5 K_4 K_3 K_2^3 K_1^2 C_{O_2} C_f$$

$$K_{22} = K_1 + K_1 K_2^{1/2} C_{O_2} + K_3 K_2 K_1^2 C_{O_2}$$

From the above equations, it is trivial to infer that the rate of change of NO concentration has complex dependencies on the concentration levels of the reacting species (NO and O_2).

2.2. Model development

The overall removal of NO in the packed tubular reactor during oxidation may be described by three mechanistic steps: (a) mass transfer from the gas phase in the packed bed to the outer surface of fibers, (b) diffusion of species within the pores, and (c) surface reaction on the surface inside the pores. The following assumptions have been made in the theoretical analysis for the development of a mathematical model to predict the removal of NO during the oxidation of NO by ACF:

(a) The temperature is uniform throughout the bed, fibers and pores. The assumption of isothermal condition was validated in the present study with the experimental measurements. Under different experimental conditions of gas flow rates and NO concentrations, the gas temperature was found to vary not more than 1 °C in either axial or radial direction.
(b) The carrier gas (N_2) is a non-adsorbing (inert) gas.
(c) Pressure drop across the bed length is negligible under the experimental conditions. This (isobaric condition) was found to be consistent with the experimental measurements made in this study for pressure drop across the packed bed.
(d) There is a constant fluid velocity throughout the bed. This assumption follows from those made in (c) above, i.e. negligible pressure-drop.

2.2.1. Mass balance in the packed bed reactor

By making a species balance in the gaseous phase in the packed bed of porosity, ε_b, the following equation is obtained:

$$\frac{\partial C_G}{\partial t} + \frac{V_z}{\varepsilon_b}\frac{\partial C_G}{\partial z} - D_z\frac{\partial^2 C_G}{\partial z^2} + \frac{(1-\varepsilon_b)}{\varepsilon_b}k_m a_f (C_G - C_f^s) = 0 \quad (15)$$

Here, C_G is the gas phase concentration of the species, at any arbitrary location z in the bed; C_f^s the concentration at the outer

surface of the fiber; V_z the gas superficial velocity in axial direction; D_z the axial dispersion coefficient; a_f the external surface area per unit volume of fiber = $2.0/R_f$; k_m is the gas film mass transfer coefficient.

The terms in Eq. (15) are transient, convection and axial dispersion terms, respectively. The last term represents mass transfer rate from the bulk gas to the surface of ACF.

2.2.2. Mass balance of NO inside the pores of fiber

The concentration of the species, C_p in the pore is obtained from the following equation:

$$\alpha\frac{\partial C_p}{\partial t} + \frac{1}{r^2}\frac{\partial}{\partial r}(r^2 N_r) + a'\frac{\partial C_s}{\partial t} = 0 \tag{16}$$

The terms in the above equation are transient, diffusion flux inside pores and surface reaction terms, and C_p is the molar concentration of component at a location r inside the pores; C_s the molar surface concentration of component inside the pores; α the intrafiber void fraction; a' the total surface area per unit volume of fiber; N_r the diffusion flux of the component in the radial direction = $-D_{eff}(\partial C_p/\partial r)$; D_{eff} is the effective diffusivity inside the pores of fibers.

2.2.3. Reaction within the pores

We observed in the experiment that the breakthrough of NO took place much earlier than the detection of NO_2 at the exit of the reactor, suggesting that the NO adsorption was rate-determining step until increase in the NO_2 concentration in the gas phase begun sharply. Similar observation was also reported elsewhere [9,10] for the oxidation of NO over ACF. Therefore, if the breakthrough time of NO_2 is t_1, we may infer that till time t_1, the overall oxidation of NO is controlled by the physical adsorption of NO, whereas after t_1, desorption of NO_2 is rate controlling. Therefore, till time t_1, assuming quasi-equilibrium between the rates of change in the surface concentration and in the gas phase concentration within the pores, we may write the rate of change of surface concentration as:

$$\frac{\partial C_s}{\partial t} = \frac{\partial C_p}{\partial t}\left(\frac{dC_s}{dC_p}\right) = S\left(\frac{\partial C_p}{\partial t}\right) \tag{17a}$$

where S is the slope of the adsorption isotherm for NO vis-à-vis ACF. The assumption of quasi-equilibrium is tantamount to saying that the change in the surface phase NO concentration due to that in the gas phase concentration is rapid or instant.

After time t_1, the rate of change of surface concentration for NO inside the pores is determined from Eq. (13) as follows:

$$\frac{\partial C_s}{\partial t} = -\frac{1}{2}\frac{\partial C_{NO}}{dt} = \frac{rc_1 C_p^2}{1 + rc_2 C_p} \tag{17b}$$

The set of governing Eqs. (15)–(17) is the basis of the model developed in this study for predicting NO concentration levels in the packed bed due to the combined effects of mass transfer and reaction kinetics. As these equations are coupled partial differential equations, independent variables being time (t), axial (z) and radial (r) distances, an approach is adopted to simplify numerical computations and significantly reduce the CPU time. Essentially, in this approach, the radial concentration profiles within the solid pores are averaged and the average gas phase concentrations within the pores of the fibers ($\overline{C}_p$) is determined. A parabolic concentration profile is assumed within the pores of fiber; an approximation, which has been found to be in good agreement with the profiles obtained from the rigorous approach. The detailed computational steps are given elsewhere [11,12] and not produced here for the sake of brevity. As a consequence of these approximations, the original partial differential Eq. (16) is reduced to the following simpler form:

$$\frac{\partial \overline{C}_p}{\partial t} - \frac{3}{R_f\alpha}k_m(C_G - C_f^s) + \frac{a'}{\alpha}\frac{\partial \overline{C}_s}{\partial t} = 0 \tag{18}$$

where

$$C_f^s = \frac{k_m C_G + 5(D_{eff}/R_f)\overline{C}_p}{(k_m + 5D_{eff}/R_f)} \tag{19}$$

Eqs. (15)–(19) are the simplified governing equations for the gas phase mass balance inside the bed and within the pores, respectively. The required initial and boundary conditions to solve Eqs. (15) and (18) are as follows:

$$t = 0; \quad C_G = \overline{C}_p = 0 \quad \text{for all } z \geq 0 \tag{20}$$

$$z = 0; \quad C_G = C_{Go}, \quad \overline{C}_p = C_{Go} \tag{21}$$

$$z = L; \quad \frac{\partial C_G}{\partial z} = \frac{\partial \overline{C}_p}{\partial z} = 0 \tag{22}$$

The aforesaid set of equations containing two dependent variables C_G and C_p as a function of time and axial location were solved simultaneously by the finite difference formulation using the NAG Fortran library (Fortran subroutine D03PCF). On a Pentium IV machine, the CPU time of computation was found to be less than a minute.

3. Experimental studies

3.1. Experimental set-up

Fig. 1 is the schematic diagram of the experimental set-up to study NO oxidation by ACF. The entire set-up may be assumed to consist of three sections: (a) gas mixing, (b) test, and (c) analytical sections. In the gas mixing section, three electronic mass flow controllers (Model PSFIC-I, Bronkhorst, The Netherlands) were used to control and measure the flow rates of N_2, O_2 and NO within the accuracy of ±0.01 slpm. A mixture of these gases of the desired concentration level was prepared by mixing three individual streams in a gas-mixing chamber (L = 135 mm and i.d. = 25 mm) made of stainless steel (SS). The various gas streams were purified using silica gel purifiers to remove any impurities or moisture in the gas. There was an option of bypassing the gaseous mixture directly to the analytical section for calibration as well as for the measurement of the inlet concentration of the gaseous mixture entering the reactor. The test section consisted of a vertical SS tubular reactor (L = 150 mm, i.d. = 14 mm) packed with ACF. The heating to the reactor was provided using heating tape (1000 W) with a

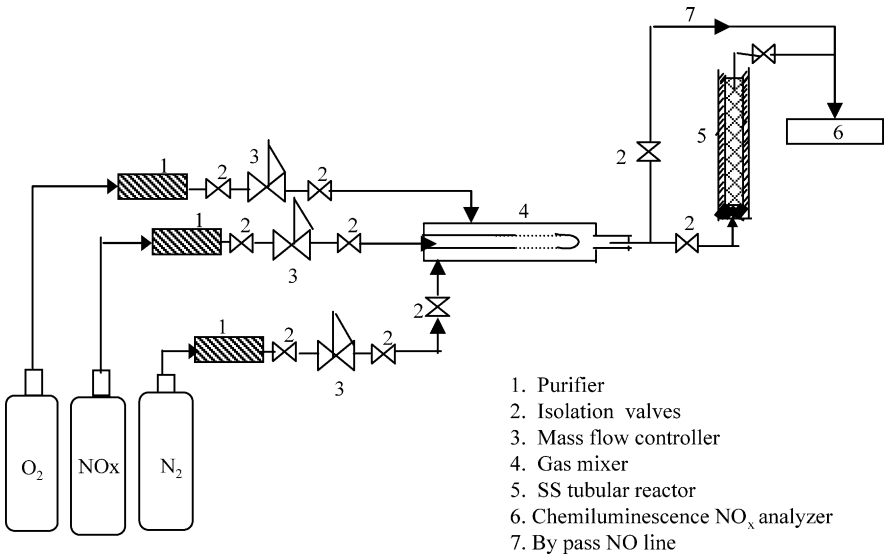

Fig. 1. Experimental set up for oxidation of NO.

thermocouple placed directly contacted with the reactor inside the wrapping. The top end of the tube was connected to the gas line using 1/4 in. swage lock fittings and especially mounted SS unions. The temperature of the column was controlled with the aid of a PID temperature controller (Model PXZ-4, Fuji Electric Co., Japan). The analytical section consisted of chemiluminescence NO_x analyzer (42C model, Thermo electron Co., USA) to measure the concentrations of NO and NO_2.

3.2. Materials

For the present study, we procured three types (different precursors) of commercial carbon fibers in activated as well as in non-activated (raw) forms. The viscose rayon and phenolic resin-based samples were procured from Beijing Evergrow Resources Co. Ltd., China and Nippon Kynol Co., Japan, respectively. The pitch-based ACF samples were procured locally. Further, the phenolic resin-based samples procured in the non-activated form were also carbonized and activated in the laboratory. The performance of the laboratory prepared ACF was compared to that of the sample procured in the activated form. The experimental set-up and detailed procedure for carbonization and activation are described in another study [13] and not reproduced here for brevity. For the reference purpose, the different ACFs used in this study, namely: viscose rayon, phenolic resin and pitch-based ACFs have been labeled as ACF1, ACF2, ACF3, respectively. The ACFs prepared from the phenolic resin-based raw fibers were labeled as ACF2-*T*X, where *T* denotes the activation temperature and X denotes activating agent, either steam (H) or CO_2 (C).

3.3. Surface characterization

The specific surface area and the pore volume of the commercial and laboratory prepared ACF samples were calculated by N_2 adsorption. The adsorption isotherms were examined using a Coulter (model no: SA 3100) BET surface area analyzer at −196 °C. The specific surface area calculated was designated as S_g. The total pore volumes (V_g) were estimated on the basis of the N_2 volume adsorbed at a relative saturation pressure (∼0.98), which actually corresponded to the total amount adsorbed. The pore size distribution (PSD) was determined based on BJH (Barrett, Joyner, and Halenda) method, which involves the area of the pore walls, and uses the Kelvin equation to correlate the relative pressure of N_2 in equilibrium with the porous solid, to the size of the pores where capillary condensation takes place [14]. Based on the data obtained on the percentage pore volume corresponding to various pore sizes calculated using the Kelvin and Halsey equations, PSD was determined following the IUPAC norms: micropores width less than 2 nm; mesopores width from 2 to 50 nm; the macrospores width greater than 50 nm [15]. The elemental analysis of C, H, N, and O of the ACF samples was carried out with the aid of a Leeman (Model CE: 440) Elemental Analyzer. The ACF samples were also examined for surface oxygen groups by the micromeritics TPD instrument (Pulse Chemisorb 2705). Pure helium at a flow rate of 0.04 slpm and the heating rate of 10 °C/min from temperature of 100–1000 °C were employed for the measurements and the evolved gases were continuously detected.

3.4. Experimental procedure

The required amount of ACF sample (∼0.25×10^{-3} kg) was accurately weighed using an electronic microbalance and pretreated before carrying out the test runs. The pretreatment was carried out by heating the samples at a temperature of ∼150 °C under vacuum (150 mmHg) for 2 h. This combination of temperature and vacuum pressure was obtained after a series of trial runs carried out to determine the optimum performance of ACF. The ACF sample was, then, packed in the SS tubular reactor wrapped with a heating tape. The reactor was heated to the desired reaction temperature and, further, kept at that temperature for another 1 h so that the system was stabilized and a uniform temperature existed in the bed. The required gas flow

rates were adjusted using the respective MFCs to obtain the desired concentrations of NO and O_2 in N_2. The exit and the inlet concentrations were measured by the Chemiluminescence NO_x analyzer.

4. Results and discussion

4.1. Surface characterization

Table 1 presents the various surface parameters including specific surface area, micropore volumes, and pore size distribution in relation to the burn-off values of various ACF samples. The samples activated with steam have higher values of burn-off as compared to those activated with CO_2 under identical activation conditions. This is due to the fact that the reaction of CO_2 is more endothermic than steam at the same temperatures. Typically at 1000 °C, the burn-off values obtained by steam activation is up to ~10% higher than that obtained by CO_2 activation. We may, also, observe from Table 1 that burn-off increases with increase in activation time and/or temperature, regardless of the type of activation agent. In addition, the BET area, total and micropore volumes of the ACF samples were observed to increase significantly with increase in the activation temperature, irrespective of the type of activation agent. For the samples activated by CO_2 at 1000 °C, the BET area was found to be 571 and 791 m^2/g for activation times of 30 and 60 min, respectively. The total and micropore volumes of these samples were measured to be 0.028, 0.012 and 0.034, 0.013 cm^3/g, respectively. However, on further increase in the activation time up to 90 min, the BET area as well as the micropore volumes decreased marginally. Table 2 compares the surface characteristics of the commercially obtained ACF samples. As observed from Table 2, the BET area, content of micropores and volume of phenolic resin-based ACF are larger than those of the viscose rayon and pitch-based samples. Table 3 summarizes the results of the elemental analysis of the samples. It may be observed that the O-content is greater (27.5%) in the steam-activated sample as compared to that (17.1%) in the CO_2-activated sample. In addition, it may be seen in Table 3 that the O-content in the commercially obtained samples is observed to be in the order: ACF1 > ACF3 > ACF2. In other words, the O-content in phenolic resin-based samples is found to be the smallest.

Table 2
Surface characteristics calculated using BET equations[a] for commercially obtained ACF samples

Sample[b]	S_g (m^2/g)	V_{micro} (cm^3/g)	V_g (cm^3/g)	PSD (%)		
				Micro	Meso	Macro
ACF1	1210	0.48	0.92	52.1	31.2	16.7
ACF2	1500	0.64	1.15	55.4	33.0	11.6
ACF3	1195	0.26	0.5	51.2	30.7	18.1

S_g: specific surface area calculated from the BET equation; V_g: total pore volume calculated from the BET equation; V_{micro}: micropore volume.
[a] The parameter estimations are done by the adsorption isotherms of N_2 gas.
[b] ACF1–3: viscose rayon, phenolic resin and pitch-based ACF, respectively.

Table 3
Elemental composition of the laboratory prepared and commercially obtained ACF samples

Sample	wt.% of the elements			
	C	H	N	O[a]
ACF2-10C	80.0	2.0	0.9	17.1
ACF2-10H	71.1	0.4	1.0	27.5
ACF1	60.0	2.3	1.1	36.6
ACF2	68.0	1.8	1.4	28.8
ACF3	66.0	2.1	0.8	31.1

10C and 10H: CO_2 and steam activated at 1000 °C, respectively; ACF1: viscose rayon based; ACF2: phenolic resin based; ACF3: pitch-based ACF samples.
[a] Oxygen content calculated by difference.

The TPD experiments were carried out to characterize the oxygen surface groups of different ACF samples. The evolved gases mainly consisted of CO_2 at low temperatures (<350 °C) due to the decomposition of strong acid groups (carboxylic and anhydride) and predominantly CO at higher temperatures (>500 °C) due to the decomposition of weak acids (lactone, phenol and carbonyl groups) [13]. Fig. 2 compares the TPD profiles of the laboratory prepared ACF2 samples activated with CO_2 and steam at 1000 °C and the commercial obtained phenolic resin ACF. As observed from the figure, the steam-activated

Table 1
Surface characteristics calculated using BET equations[a] for laboratory prepared phenolic resin-based ACF samples

Sample	Activation time (min)	Burn-off (wt. %)	S_g (m^2/g)	V_{micro} (cm^3/g)	V_g (cm^3/g)	PSD (%)		
						Micro	Meso	Macro
ACF2-10C	30	56.3	571	0.012	0.028	44.0	32.5	23.5
	60	58.6	791	0.013	0.034	40.1	38.2	21.7
	90	65.6	702	0.011	0.029	37.1	34.7	28.2
ACF2-9C	30	48.5	459	0.007	0.020	32.5	31.1	36.4
ACF2-8C	30	40.6	205	0.002	0.015	27.8	30.3	41.9
ACF2-10H	30	66.1	928	0.039	0.089	44.2	32.5	23.3
ACF2-9H	30	52.5	688	0.008	0.024	33.6	32.9	33.5
ACF2-8H	30	45.6	615	0.004	0.014	30.3	29.8	39.9

S_g: specific surface area calculated from the BET equation; V_g: total pore volume calculated from the BET equation; V_{micro}: micropore volume; 8C, 9C and 10C: CO_2 activated at 800, 900 and 1000 °C, respectively; 8H, 9H and 10H: steam activated at 800, 900 and 1000 °C, respectively.
[a] The parameter estimations are done by the adsorption isotherms of N_2 gas.

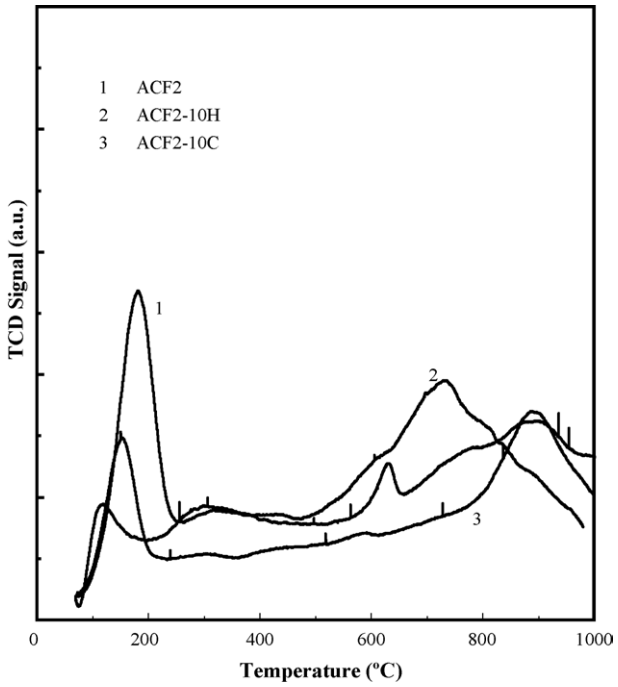

Fig. 2. TPD profiles of laboratory prepared ACF samples.

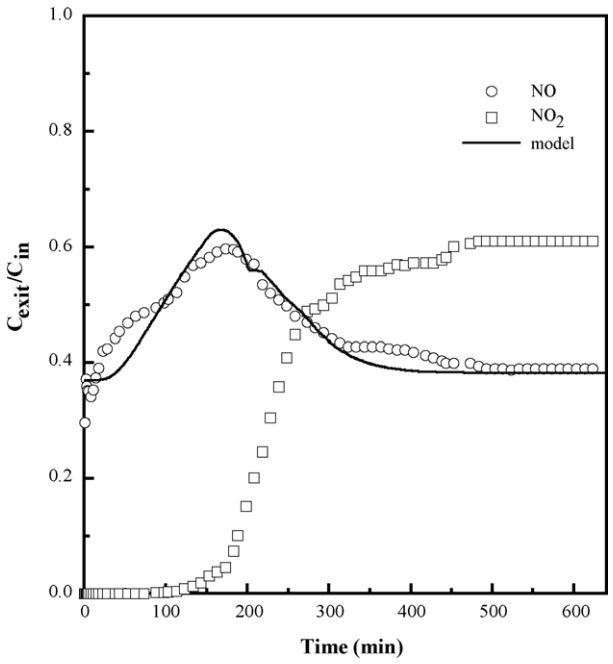

Fig. 4. Breakthrough profiles of NO over pitch-based ACF ($T = 30\,^{\circ}C$, $W = 0.25 \times 10^{-3}$ kg, $Q = 0.2$ slpm, $C_{NO} = 250$ ppm and $C_{O_2} = 20\%$).

sample has higher oxygen surface groups than that activated with CO_2. Fig. 3 shows the TPD profiles of the commercial obtained samples. We may observe in the figure that the viscose rayon-based ACF has both CO_2 and CO evolving groups. On the other hand, phenolic resin and pitch-based ACF samples have only CO evolving groups present on their surfaces. The extent of various oxygen functional (CO_2 and CO evolving) groups was found to be in the following order: ACF1 > ACF3 > ACF2.

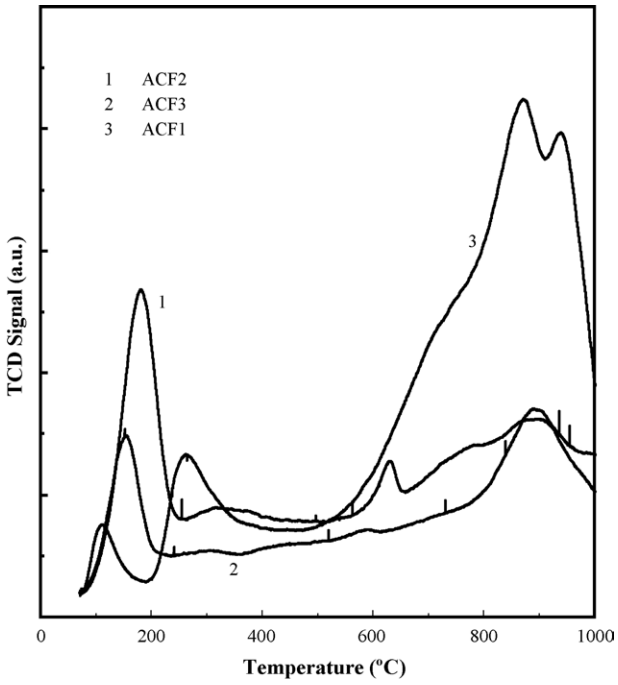

Fig. 3. TPD profiles of commercial ACF samples.

4.2. NO oxidation over ACF

The experimental transient data obtained during the oxidation of NO are presented in Figs. 4–12. The data obtained using the NO_x analyzer represent the breakthrough curves (transient response of the adsorbent bed to a step-change in the influent concentration) for NO and NO_2 during the oxidation of NO. The steady-state conversion of NO is defined as $(C_{inlet} - C_{exit\,NO})/C_{inlet}$ or $C_{exit\,NO_2}/C_{inlet}$, where C_{inlet} is the inlet concentration of NO. We, also, measured separately the concentrations of the reaction by-products CO, CO_2, N_2O in a few selective experiments, using gas chromatography, wherein we observed no significant formation of these gaseous products. In none of the cases, total concentration of these compounds was observed more than 1%. This is due to the fact that the reactions were carried out at room temperature (30 °C). At low temperatures, possibility of the formation of the above-mentioned gaseous by-products is minimal.

Fig. 4 illustrates the breakthrough profiles obtained during NO oxidation over the pitch-based ACF. Oxidation was carried out in the presence of O_2 (20%, v/v) and at a reaction temperature of 30 °C. The inlet NO and total gas flow rate were kept constant at 250 ppm and 0.2 slpm. As observed from the figure, breakthrough of NO occurred instantaneously. Following breakthrough, the exit NO concentration increased up to the maximum value of 60% (relative to inlet concentration) before subsequently decreasing up to the steady-state level of 38%. The most important aspect of the result shown in Fig. 4 is that for the time interval during which NO concentration is rising, the produced NO_2 is adsorbed completely. Till about first 120 min, no breakthrough of NO_2 was observed. At around 130 min, the concentration of NO reached its maximum value. Around the same

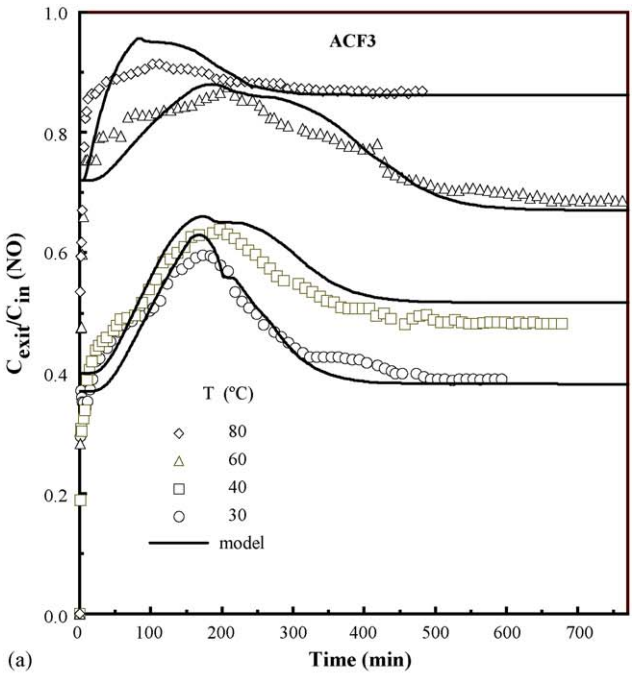

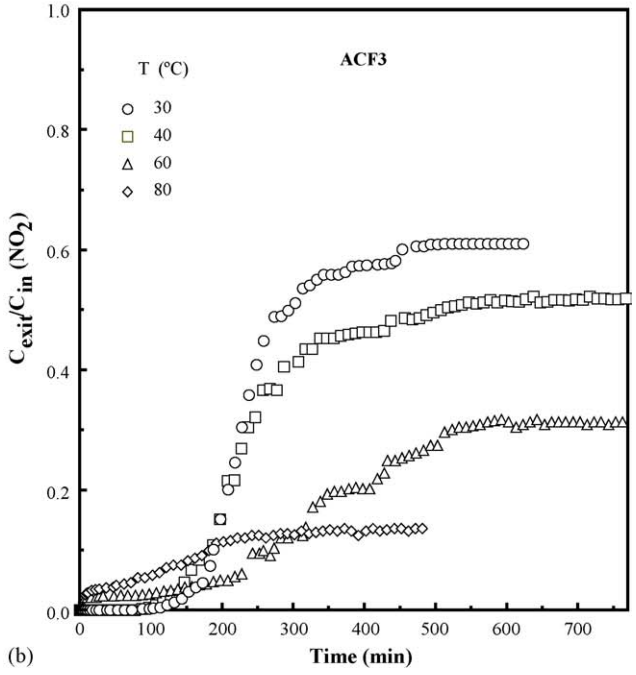

Fig. 5. (a) NO breakthrough: effects of reaction temperatures ($W = 0.25 \times 10^{-3}$ kg, $Q = 0.2$ slpm, $C_{NO} = 250$ ppm and $C_{O_2} = 20\%$) and (b) NO_2 breakthrough: effects of reaction temperatures ($W = 0.25 \times 10^{-3}$ kg, $Q = 0.2$ slpm, $C_{NO} = 250$ ppm and $C_{O_2} = 20\%$).

time breakthrough of NO_2 occurred. As observed the steady-state conversion of NO (or the exit concentration of NO_2) was ~62%.

We may explain the breakthrough characteristics of NO and NO_2 with the aid of the proposed mechanism discussed in Section 2.1. The sharp rise in the outlet concentration of NO during the initial period indicates that the physical adsorption and desorption of NO i.e. step (a) of mechanism 1 or mechanism 2 is slower compared to the remaining steps, which are quite rapid,

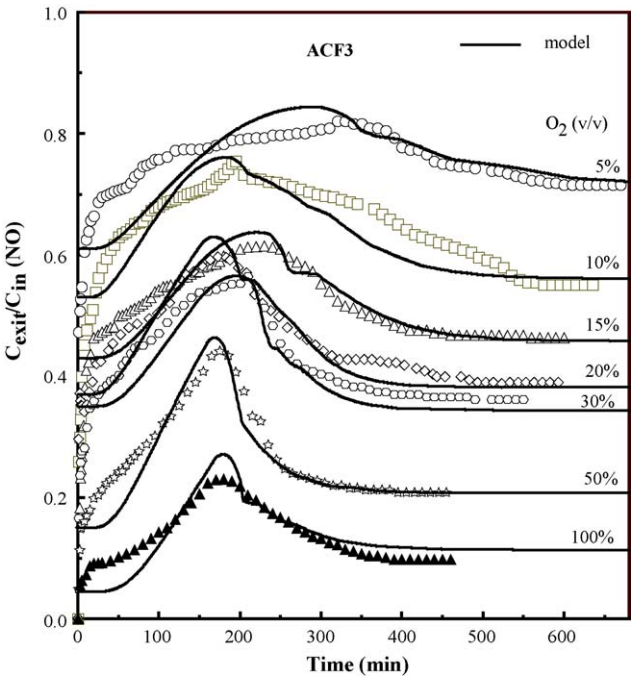

Fig. 6. NO oxidation: effects of O_2 concentrations ($T = 30\,^{\circ}C$, $W = 0.25 \times 10^{-3}$ kg, $Q = 0.2$ slpm and $C_{NO} = 250$ ppm).

i.e. at quasi-equilibrium conditions. Therefore, during the initial period the adsorption of NO is the rate-determining step. When the bed begins to saturate with NO and/or NO_2, we may observe large increase in the outlet concentration of NO, which reaches to a maximum value. At the same time breakthrough of NO_2 occurs, which results in the vacant sites, consistent with the reaction step (f) of mechanism 1, or (e) of mechanism 2. Hence, adsorption of NO may again take place on these vacant sites,

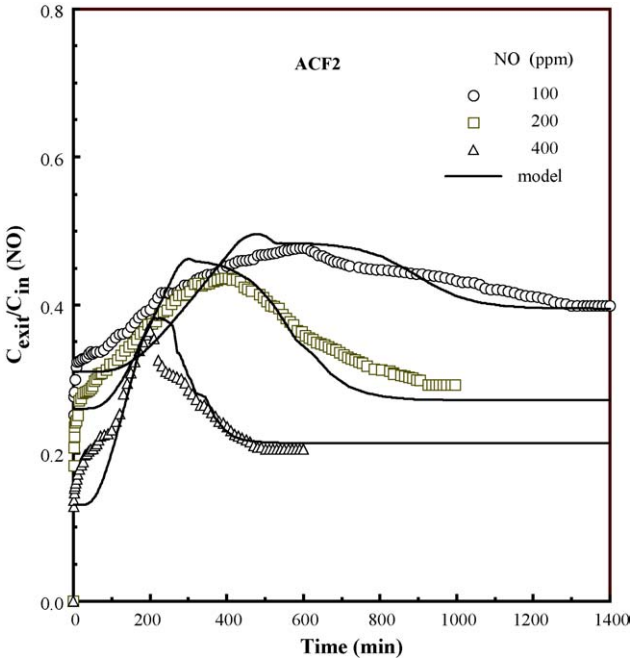

Fig. 7. NO oxidation: effects of NO concentrations ($T = 30\,^{\circ}C$, $W = 0.25 \times 10^{-3}$ kg, $Q = 0.2$ slpm and $C_{O_2} = 20\%$).

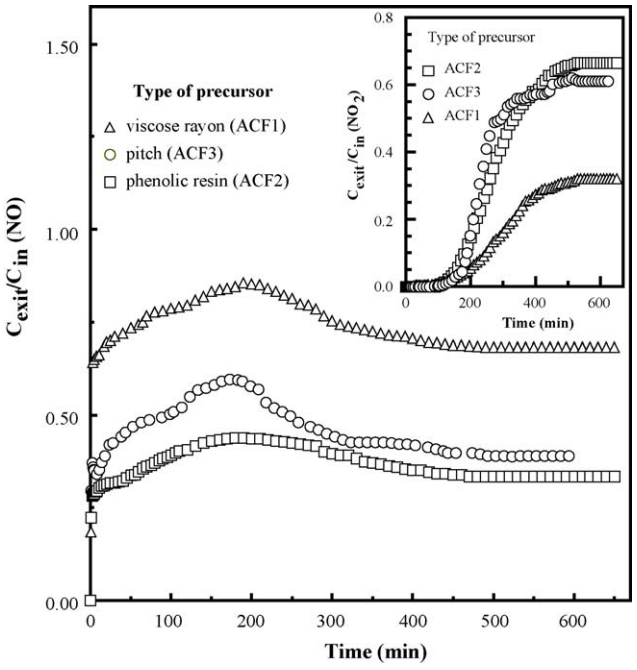

Fig. 8. NO oxidation: precursors effects ($T = 30\,^{\circ}C$, $W = 0.25 \times 10^{-3}$ kg, $Q = 0.2$ slpm, $C_{NO} = 250$ ppm and $C_{O_2} = 20\%$).

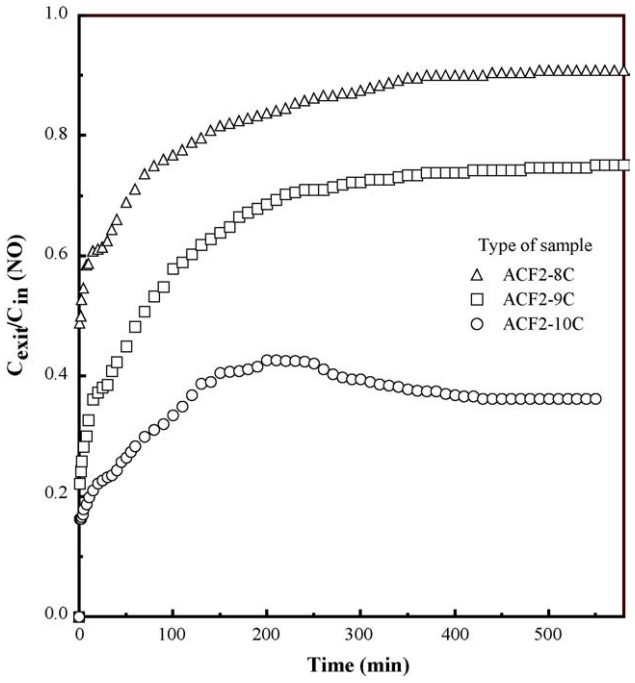

Fig. 10. Effect of activation temperature on the oxidation of NO ($T = 30\,^{\circ}C$, $W = 0.25 \times 10^{-3}$ kg, $Q = 0.2$ slpm, $C_{NO} = 250$ ppm and $C_{O_2} = 20\%$).

so that there will be a gradual decrease in the outlet concentration of NO before reaching the steady-state level. Adsorption of NO on the new vacant sites may proceed only when NO_2 is desorbed to release these sites, which then becomes the slower step. Therefore, during this time period desorption of NO_2 is the rate-limiting step, i.e. the step (f) of mechanism 1 or (e) of mechanism 2. As pointed out earlier in the text, the extent of physical adsorption of NO on activated carbons is generally very low as pointed out previously. It is also important to note that the role of ACF in the present context is of a catalyst, rather than an adsorbent, since the steady-state concentration level of NO remains below that at the inlet, as the ACF sites are continuously recovered following the desorption of NO_2 from the

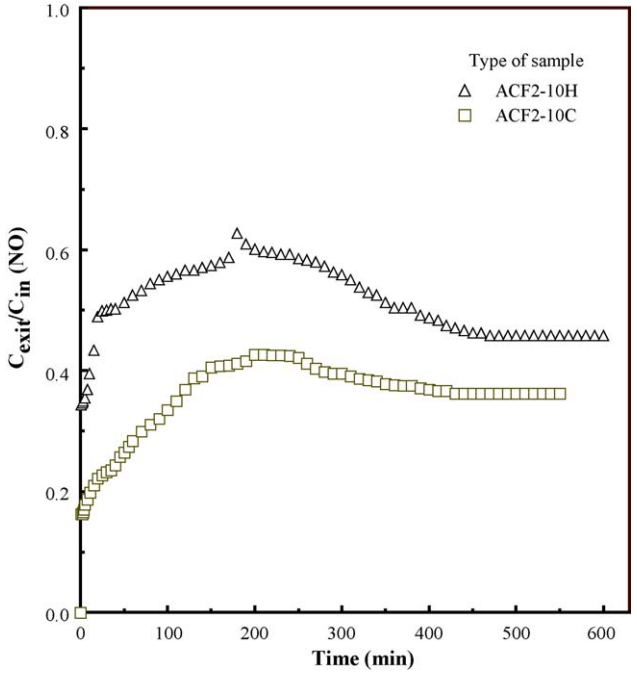

Fig. 9. Effect of activating agents on the oxidation of NO ($T = 30\,^{\circ}C$, $W = 0.25 \times 10^{-3}$ kg, $Q = 0.2$ slpm, $C_{NO} = 250$ ppm and $C_{O_2} = 20\%$).

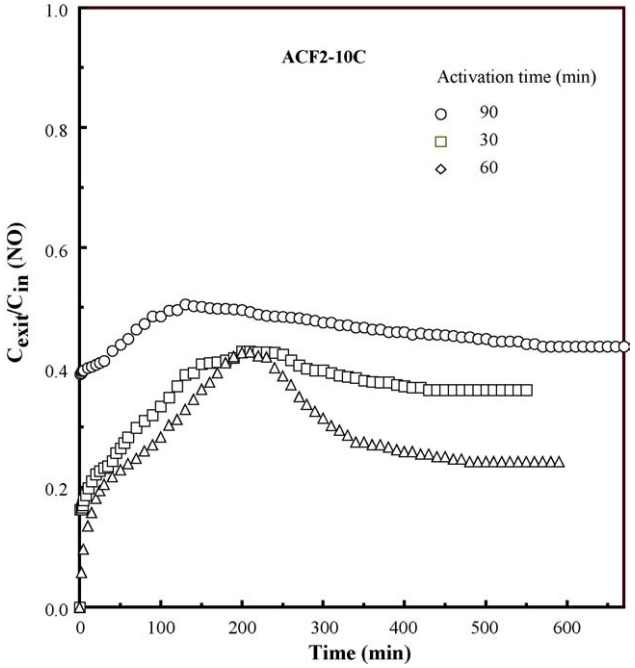

Fig. 11. Effect of activation time on the oxidation of NO ($T = 30\,^{\circ}C$, $W = 0.25 \times 10^{-3}$ kg, $Q = 0.2$ slpm, $C_{NO} = 250$ ppm and $C_{O_2} = 20\%$).

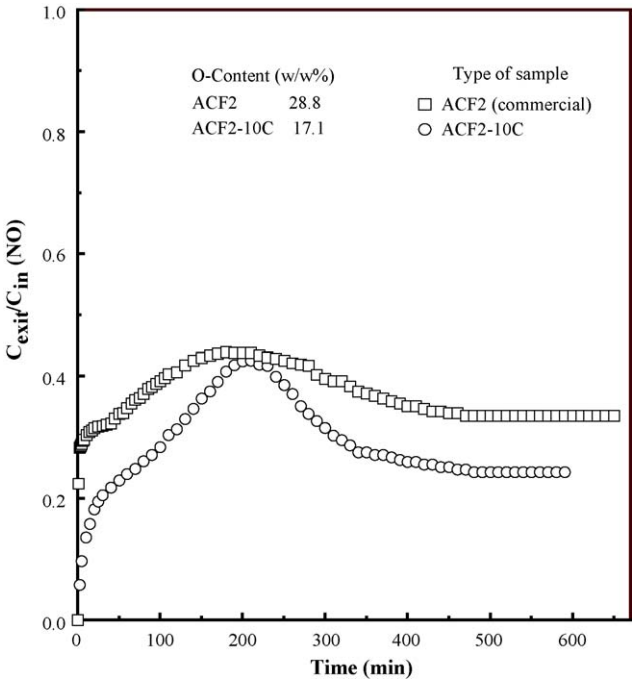

Fig. 12. Comparative performance of lab prepared vs. commercial ACF ($T = 30\,^{\circ}C$, $W = 0.25 \times 10^{-3}$ kg, $Q = 0.2$ slpm, $C_{NO} = 250$ ppm and $C_{O_2} = 20\%$).

surface. For the present case, the following reaction mechanism may schematically be postulated:

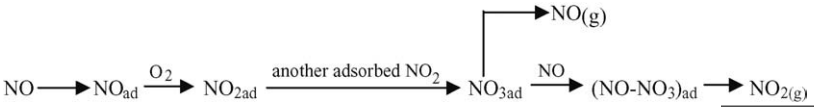

Fig. 4 also presents the model predicted breakthrough curve of NO along with the corresponding experimental data under the identical operating conditions. In the model prediction of the breakthrough curves, Eq. (17a) was used to calculate the rate of change of the surface concentration of NO inside the pores till breakthrough of NO_2 occurred. For the time-period following the breakthrough of NO_2, Eq. (17b) was used to calculate the concentration of NO in the packed bed. The slope of linear isotherm (S) and the reaction rate constants (rc_1 and rc_2) were used as the adjustable parameters in the model. The effective pore diffusivity (D_{eff}) was calculated to be 2.9×10^{-8} m^2/s as per the procedure described in Appendix A. The numerical value of D_{eff} is in the same order of magnitude as reported elsewhere for the pore-diffusion of toluene as well as SO_2 in ACF [15,16]. At the gas flow rate of 0.2 slpm, Re (based on the fiber diameter of 2.8×10^{-6} m) and Sc were calculated to be 0.0085 and 0.014, respectively. Under these conditions, Sh was calculated to be 2.015, which in turn was used to calculate the gas film mass transfer coefficient, k_m (652.8 m/s) (see Appendix A for correlations). The relatively larger value of k_m suggests the insignificant diffusional (particle) resistance in the bed packed with ACF. Single values of S, rc_1 and rc_2, adjusted at 0.023 m^3/kg, 1.4×10^{-6} m^3/mol s and 38.2 m^3/mol, respectively, were used to get the best-fit curve to the experimental data.

4.2.1. Effect of reaction temperature

Experiments were carried out at varying reaction temperatures over the range between 30 and 80 °C to ascertain the temperature at which the maximum oxidation of NO occurs on ACF. The corresponding breakthrough curves obtained during the oxidation of NO are shown in Fig. 5a and b. All experiments were carried out on the fixed amount (0.25×10^{-3} kg) of ACF (pitch based) and under constant gas flow rate (0.2 slpm). The inlet NO and O_2 concentrations were also set constant at 250 ppm and 20% (v/v), respectively. As observed from Fig. 5a, breakthrough of NO occurred immediately and the initial rise in the outlet concentration of NO was observed to increase with increase in the reaction temperature. This may be attributed to the fact that the extent of the physical adsorption of NO decreases with increase in the temperature. Hence, with increase in the reaction temperature, the maximum concentration levels increased. For example, the maximum concentrations attained at 30 and 80 °C were ~60 and ~90% (relative to the inlet concentration), respectively. The corresponding steady-state concentrations were measured to be 0.38 and 0.87. Contrary to NO, breakthrough of NO_2 occurred after relatively longer time (130 min) as observed from Fig. 5b. The steady-state conversion was observed to be ~62% at 30 °C. As the reaction temperature was raised to 40 °C, the breakthrough time of NO_2 as well as the steady-state conversion decreased to 100 min and ~52%, respectively. Further rise in the reaction temperature up to 80 °C reduced the breakthrough time to 9 min and steady-state conversion to ~13%. This suggests that the catalytic activity of ACF for the oxidation of NO gradually decreases with increase in the reaction temperature. Thus, a reaction temperature of 30 °C (~room temperature) was found to be favorable for the maximum oxidation of NO.

Fig. 5a also compares the model predicted breakthrough curves (NO) with the corresponding experimental data under identical operating conditions. At 30 °C, the slope of the isotherm (S) was required to be adjusted at 0.023 m^3/kg, whereas at 80 °C the parameter was adjusted at 0.005 m^3/kg. For the remaining temperatures as well, the adjusted values for S were found to decrease with increase in temperature. The gradual decrease in the slope of the equilibrium isotherm from 0.023 to 0.005 m^3/kg with increase in the reaction temperature from 30 to 80 °C is consistent with the typical adsorption/desorption characteristics of an adsorbate vis-à-vis adsorbent, i.e. the adsorbed amount decreases with increase in temperature. The rate parameters rc_1 and rc_2 at 80 °C were adjusted at 0.08×10^{-6} m^3/mol s and 18.2 m^3/mol, respectively, smaller than the corresponding values at 30 °C (1.4×10^{-6} m^3/mol s and 38.2 m^3/mol, respectively). Referring Eqs. (9)–(12) and (14), rc_1 and rc_2 have complex dependencies on temperature via individual equilibrium constants. Nonetheless, the values of the rate parameters were found to decrease with increasing temperatures over the range between 30 and 80 °C.

4.2.2. Effect of O_2 concentration

Fig. 6 illustrates the effect of O_2 concentration on the oxidation of NO. The O_2 concentration was varied in the range between 5% and approximately 100% (v/v) keeping the inlet NO concentration constant at 250 ppm. The reaction temperature and total gas flow rate (O_2 + N_2 + NO) were also kept constant at 30 °C and 0.2 slpm. Both the maximum and steady-state concentrations of exit NO were observed to decrease with increasing O_2 concentrations. At 5% (v/v) O_2 concentration, the steady-state conversion (or $1 - C_{exit}/C_{inlet}$) was ∼28%, while at ∼100% (v/v) concentration, i.e. pure O_2, NO conversion was ∼90%. Although the results suggested gradual improvement in the conversion of NO with increase in O_2 concentration, the concentration of O_2 in the remaining experiments carried out in this work was kept constant at 20% (v/v) to simulate the atmospheric O_2 concentration level (∼21%) in the reaction mixture. With increase in the O_2 concentration, breakthrough time of NO_2 as well as the time to achieve stationary concentration also decreased. For the sake of brevity, the corresponding breakthrough profiles of NO_2, similar to those shown on Fig. 5b, are not presented in this paper and are only qualitatively discussed. For example, breakthrough of NO_2 occurred at 240 and 70 min for 5 and ∼100% (v/v) O_2 concentrations, respectively. Fig. 6 also describes the model predicted breakthrough curves at various O_2 concentration levels under identical experimental conditions. For O_2 concentration of 5% (v/v) the values of rc_1 and rc_2 in the model prediction were adjusted at 0.18×10^{-6} m^3/mol s and 9.2 m^3/mol, respectively, whereas for ∼100% (v/v) O_2, these values were increased to 19.8×10^{-6} m^3/mol s and 48.2 m^3/mol. For the remaining O_2 concentrations as well, the adjusted values for rc_1 and rc_2 were required to be increased with increase in the concentration, which is qualitatively consistent with Eqs. (9)–(12) and (14). In the model, the values of S were marginally adjusted over the range between 0.019 and 0.021 m^3/kg to fit the breakthrough curves of Fig. 6. Considering the insignificant concentration of NO (250 ppm) in comparison to the O_2 concentration in the reacting gaseous mixture, the nearly unchanged value of the slope of the equilibrium isotherm obtained for various O_2 concentrations is consistent with the basic physics.

4.2.3. Effect of inlet NO concentrations

To observe the effects of NO inlet concentration on the oxidation of NO, the experiments were carried out for varying NO concentrations: 100, 200 and 400 ppm. Oxidation was carried out on the phenolic resin-based ACF (0.25×10^{-3} kg) in the presence of O_2 (20%, v/v) and at a temperature of 30 °C. The total gas flow rate was kept constant at 0.1 slpm. Fig. 7 describes the breakthrough profiles of NO obtained during oxidation. As observed from the figure, time to reach maximum concentration of NO decreased with increase in NO concentration. In addition, the maximum NO concentration level also decreased. On the other hand, the breakthrough time of NO_2 was observed (data not shown here for brevity) to decrease from 350 to 110 min with the increase in the NO concentration from 100 to 400 ppm. The corresponding steady-state conversions were observed to be 60, 70 and 80%, respectively. Fig. 7 also shows the model predicted breakthrough curves at various inlet NO concentrations, which are in good agreement with the experimental data. In the model predictions, the values of S, rc_1 and rc_2 were expectedly set constant (independent of NO concentration in accordance with Eqs. (9)–(12) at 0.020 m^3/kg, 0.48×10^6 m^3/mol s, and 3.22×10^{-3} m^3/mol, respectively.

4.2.4. Effect of precursors (commercially available ACFs)

Several experiments were carried out on three different precursors-based ACFs, namely: viscose rayon, phenolic resin and coal tar pitch, to examine the effect of precursors on the oxidation of NO. In each test run, the inlet NO and O_2 concentrations were kept constant at 250 ppm and 20% (v/v), respectively. The total gas flow rate and reaction temperature were set at 0.2 slpm and 30 °C, respectively. The corresponding breakthrough profiles of NO and NO_2 are shown in Fig. 8 and the inset of the same, respectively. As observed from the figure, the performance of the rayon-based ACF is relatively inferior as compared to that of the phenolic resin and pitch-based ACFs. As also observed, the breakthrough time of NO_2 for rayon-based ACF was 60 min, with the steady conversion of NO obtained at ∼32%. On the other hand, although the difference in breakthrough times of NO_2 for pitch and phenolic resin ACFs were marginal, conversion was relatively higher for the phenolic resin-based ACF. The breakthrough time and conversion for pitch and phenolic resin-based ACFs were observed to be 130 and 120 min, and 61 and 67%, respectively. The difference in the overall performances of three ACFs was attributed to the combined influences of BET area, micropore volume and the specific oxygen functional groups on the surface of each ACF. Referring Table 2, the BET area and micropore volume of the phenolic resin-based ACF sample are 1500 m^2/g and 0.64 cm^3/g, respectively, whereas these values for the pitch and viscose rayon samples are 1195 m^2/g, 0.26 cm^3/g and 1200 m^2/g, 0.48 cm^3/g, respectively. As also seen from the table, the phenolic resin-based ACF has the largest proportions of micro- and mesopores and lowest number of macropores. Revisiting Fig. 3 on the comparison of the TPD profiles of different ACFs, one may observe that the extent of surface oxygen (CO_2 and CO evolving) functional groups is relatively lower in the phenolic resin-based ACF as compared to that in the pitch and rayon-based ACFs. Based on these results the higher conversion of NO on phenolic ACF may be attributed to the higher BET area as well as higher micropore volume than those for the other two ACFs. However, this is not true for the pitch-based sample because BET area and micropore volume of the pitch-based ACF are smaller than those of the viscose rayon ACF. Therefore, it may be inferred that BET area and micropore volumes are not the primary factors affecting the oxidation of NO. The results indicate that the effect of the surface oxygen groups on the oxidation of NO is predominant over that of the porous texture. Therefore, we may conclude that lesser the oxygen groups on ACF, higher the conversion of NO. As shown on Fig. 3, significant differences exist between the amounts of CO evolved groups on those three samples. In particular, phenolic resin sample has relatively very lower CO evolving groups compared to pitch and viscose rayon samples. On the other hand viscose rayon sample contains more CO evolving groups.

4.2.5. Effect of activating agents

Fig. 9 presents the breakthrough profiles of NO obtained during the oxidation of NO on the steam and CO_2-activated ACF2 samples. As observed, the initial rise in the outlet concentration of NO for the steam-activated sample was relatively higher than that for the CO_2-activated sample. The corresponding maximum values attained for the steam and CO_2-activated samples were 63 and 43% (relative to inlet concentration), respectively. On the other hand, breakthrough of NO_2 occurred more or less at the same time for both samples, but the steady-state conversions were found to be 64 and 54% for the CO_2 and steam-activated samples, respectively. The difference in the conversions may again be attributed to the difference in the amount of CO evolving surface groups rather than difference in the BET area. As one may see from Table 1, the BET area of CO_2-activated ACF2 was smaller (571) than that (928) of the steam-activated ACF2. However, re-referring Fig. 2, it may be observed that the CO_2-activated sample has lower CO evolving groups compared to those of the steam-activated sample. The conversion data are consistent with the extent of the O_2 surface groups on the ACF.

4.2.6. Effect of activation temperature

Fig. 10 compares the breakthrough curves for the ACF samples prepared at different activation temperatures. The oxidation conditions are mentioned in the figure. As observed, the initial rise in the exit concentration of NO was found to be the smallest for the ACF sample activated at 1000 °C and maximum for the sample activated at 800 °C. In addition, for the former sample the exit NO concentration increased up to a maximum level followed by subsequent decrease up to the steady-state level, whereas this trend was not observed for the samples activated at low temperatures i.e. at 900 and 800 °C. The exit NO concentration continuously increased and reached steady-state levels at 76 and 91% (relative to inlet concentration), respectively for the samples activated at 900 and 800 °C. The variation in the NO conversion or the exit concentration at three activation temperatures is explained with the help of the BET area and micropore volumes of the samples reported in Table 1. The BET area of the sample activated at 800 °C (ACF2-8C) increased from 205 to 571 m^2/g with increase in the activation temperature up to 1000 °C. In addition, the micropore volume increased from 0.002 to 0.012 cm^3/g, respectively for the samples activated at 800 and 1000 °C, suggesting that the improved breakthrough time of NO_2 and conversion for ACF2-10C sample are in essence due to relatively larger BET area as well as micropore volume.

4.2.7. Effect of activation time

To determine the required activation time, the carbon fibers were activated with CO_2 at 1000 °C for different times ranging between 30 and 90 min. These laboratory prepared ACFs were, then, used in the oxidation experiment under the identical conditions as described for the data presented in Fig. 10. The corresponding breakthrough profiles obtained during the oxidation of NO for the samples activated for various times are shown in Fig. 11. As observed, the sample activated for more than 60 min was found to be inferior in comparison to the remaining samples. With increase in the activation time from 30 to 60 min, the maximum concentration level was found to be approximately the same (42% relative to the inlet concentration), with marginal difference observed in the initial rise of the exit concentration of NO. In addition, for both (30 and 60 min activated) samples, peak in NO concentration occurred at the same time (210 min). On the other hand, breakthrough time of NO_2 was observed to first increase for the samples activated between 30 and 60 min, whereas for the sample activated for 90 min breakthrough time decreased. For instance, breakthrough occurred at 110 min for 30 min-activated sample and increased to 160 min for 60 min-activated sample. For the sample activated for 90 min the breakthrough time decreased to 80 min. The corresponding steady-state conversions were found to be 63, 76 and 56% for the samples activated for 30, 60 and 90 min, respectively. The difference in the performance of these samples may be attributed to combined influences of the BET area and micropore volume. As seen in Table 1, the BET area and micropore volumes are relatively higher for the samples activated for 60 min than those of the samples activated for 30 and 90 min. This finding suggests that the improved performance of the former sample is due to the relatively larger BET area and micropore volume.

4.2.8. Comparative performance of lab prepared versus commercial ACF

Fig. 12 compares the oxidation behavior of the laboratory prepared phenolic resin-based ACF sample (ACF2-10C) with that of the commercial ACF. The laboratory prepared sample was activated with CO_2 at 1000 °C for 60 min. The breakthrough profiles of two samples showed that the initial rise in NO concentration was lower for the laboratory prepared sample in comparison to that for the commercial sample. However, the maximum NO concentration levels were observed to be nearly the same for both samples. The steady-state conversions were obtained as 76 and 67%, respectively for two samples. The overall superior performance of the lab prepared ACF over the commercial sample may be attributed to the relatively lesser extent of O_2 functional groups on the former sample. As seen from the TPD profiles (Fig. 2), there is no significant difference in the extents of oxygen functional groups, in particular CO evolving groups, present on two samples. However, on the elemental analysis of the samples, the O-content was indeed found to be larger (28.8%, w/w) for commercial sample as compared to that (17.1%) for the lab prepared sample, suggesting the presence of O-contents on the carbon surface in groups other than CO. The data for the O-contents obtained for two samples are reported in Fig. 12.

5. Conclusions

The steady-state NO conversion was observed to vary between 10 and 90% (relative to the inlet concentration) during the catalytic oxidation of NO on ACF carried out in a tubular reactor. The extent of conversion depended upon the reaction temperature, inlet O_2 and NO concentrations, and the types and the methods of preparing ACF. The phenolic resin-based ACF was found to be more effective in the oxidation of NO in comparison to the pitch and viscose rayon-based ACFs. Similarly,

the performance of the ACF activated by CO_2 at 1000 °C for 60 min was observed to be superior to that of the ACF activated by steam under identical activation conditions. The difference in the performance of the ACF samples was attributed to the combined influence of the presence of the amounts of the CO evolving surface O_2 functional groups, BET area and micropore volume of the ACF. A kinetic mechanism for the oxidation of NO was proposed consisting of adsorption followed by the oxidation of NO into NO_2, formation of intermediates such as NO_3 and NO–NO_3, and finally, desorption of NO_2. A mathematical model was developed to explain the experimental breakthrough data, incorporating the effects of mass transfer resistance in the ACF bed and within the pores of the ACF, along with the surface reactions. The model predictions were observed to be in good agreement with the data.

Acknowledgements

The authors acknowledge the partial financial support (Grant no.: F-26-4/2002/71, 31 March 2003) from the ministry of Human Resources and Development (MHRD), New Delhi to conduct this study. The authors also thankfully acknowledge Nippon Kynol Inc., Japan and Beijing Evergrow Resourses Co. Ltd., China for supplying the ACF samples.

Appendix A

A. The axial dispersion co-efficient in the packed bed, D_z is correlated with particles Reynolds number, Re and Schmidt number, Sc through the empirical correlation [17]:

$$D_z = \frac{D_m}{\varepsilon_b}(20 + 0.5ScRe)$$

B. The mass transfer co-efficient k_m in the packed bed is calculated using the following correlation for Sherwood number defined as, $Sh = 2k_m r_{pore}/D_m$ [17]:

$$Sh = 2.0 + 1.1(Sc)^{0.33}(Re)^{0.6}$$

C. The effective diffusivity inside the pores is determined using the formula $D_{eff} = \alpha D_{comb}/\tau$; where the combined diffusivity, D_{comb} inside the micropores of the ACF is given by the combination of Knudsen (D_k) and molecular (D_m) diffusivity. The Knudsen diffusivity is given by:

$$D_k = 97 r_{pore}\left(\frac{T}{M}\right)^{1/2} \text{m}^2/\text{s}$$

where r_{pore} is the pore radius in m, M the molecular weight in g/mol, T is the temperature in K. The combined diffusivity contributed by molecular and Knudsen diffusivities is given by $1/D_{comb} = (1/D_k) + (1/D_m)$.

References

[1] J. Muniz, J. Marban, A.B. Fuertes, Low temperature catalytic reduction of NO over polyarylamide-based carbon fibers, Appl. Catal. B: Environ. 23 (1999) 25–35.
[2] K. Murata, K. Kaneko, H. Kanoh, D. Kasuya, K. Takahashi, F. Kokai, M. Yudasaka, S. Iijima, Adsorption mechanism of supercritical hydrogen in internal and interstitial nanospaces of single-wall carbon nanohorn assembly, J. Phys. Chem. B 106 (2002) 11132–11138.
[3] Y.-W. Lee, D.-K. Choi, J.-W. Park, Performance of fixed-bed KOH impregnated activated carbon adsorber for NO and NO_2 removal in the presence of oxygen, Carbon 40 (9) (2002) 2605–2611.
[4] Y. Kong, C.Y. Cha, NO_x adsorption on char in presence of oxygen and moisture, Carbon 34 (8) (1996) 1027–1033.
[5] N. Shirahama, S.H. Moon, K.H. Choi, T. Enjoji, S. Kawano, Y. Korai, M. Tanoura, I. Mochida, Mechanistic study of adsorption and reduction of NO_2 over activated carbon fibers, Carbon 40 (2002) 2605–2611.
[6] A. Claudino, J.L. Soares, R.F.P.M. Moreira, H.J. Jose, Adsorption equilibrium and breakthrough analysis for NO adsorption on activated carbons at low temperatures, Carbon 42 (8–9) (2004) 1483–1491.
[7] J.K. Neathery, A.M. Rubel, J.M. Stencel, Uptake of NO_x by activated carbons: bench-scale and pilot-plant testing, Carbon 35 (9) (1997) 1321–1327.
[8] J. Yang, G. Mestl, D. Herein, R. Schlogl, J. Find, Reaction of NO with carbonaceous materials 1. Reaction and adsorption of NO on ashless carbon black, Carbon 38 (5) (2000) 715–727.
[9] I. Mochida, N. Shirahama, S. Kawano, Y. Korai, A. Yasutake, M. Tanoura, S. Fujii, M. Yoshikawa, NO oxidation over activated carbon fiber (ACF). Part 1. Extended kinetics over a pitch-based ACF of very large surface area, Fuel 79 (2000) 1713–1723.
[10] I. Mochida, Y. Kawabuchi, S. Kawano, Y. Matsumura, M. Yoshikawa, High catalytic activity of pitch-based activated carbon fibers of moderate surface area for oxidation of NO to NO_2 at room temperature, Fuel 76 (6) (1997) 543–548.
[11] S. Adapa, V. Gaur, N. Verma, Activated carbon fibers (ACFs) for the control of NO_x emissions, in: Proceedings of First Indo–US Joint Conference of IIChE and AIChE 2004, Mumbai, India, December 28–30, 2004.
[12] D. Das, V. Gaur, N. Verma, Removal of volatile organic compound by activated carbon fiber, Carbon 42 (2004) 2949–2962.
[13] V. Gaur, A. Sharma, N. Verma, Preparation and characterization of ACF for the adsorption of BTX and SO_2, Chem. Eng. Process 45 (2006) 1–13.
[14] S.J. Gregg, K.S.W. Singh, Adsorption, Surface Area and Porosity, 2nd ed., Harcourt Brace Javanovich, London, UK, 1982.
[15] T. Cheng, Y. Jiang, Y. Zhang, S. Liu, Prediction of breakthrough curves for adsorption on activated carbon fibers in a fixed bed, Carbon 42 (15) (2004) 3081–3085.
[16] V. Gaur, N. Verma, Removal of SO_2 by activated carbon fibers impregnated with transition metals, communicated.
[17] R.T. Yang, Gas Separation by Adsorption Processes, 1st ed., Imperial College, UK, 1997.